Smart Blade Flutter Alleviation

Reza Moosavi

School of Physics, Engineering & Computer Science, University of Hertfordshire, Hatfield, AL10 9AB, UK

Abstract: In this paper, the effect of using a piezoelectric material has been shown on postponing the flutter phenomenon on a regular blade. System response of a smart blade with only flapwise and edgewise plunge DOF shows that the oscillations of the smart blade can be effectively decayed in a very short time by using efficient piezopatches in the flapwise and edgewise plunge DOF. Furthermore, in a smart blade with four DOF, it has been indicated having piezopatches in flapwise and edgewise plunge DOF can defer the flutter speed 81.41% which is a noticeable increase in the flutter speed. Finally, by adding a piezopatch to the pitch DOF to a smart blade, it is possible to postpone the flutter speed 155% which is a very considerable increase.

Keywords: piezoelectric material, flutter, smart blade

1. Introduction

In modern blade, due to high flexibility, aeroelastic analysis is crucial. To maximize the blade aerodynamic performance, it is very important to control aeroelastic instability [1, 2]. Flutter phenomenon is one significant aeroelastic analysis. Flutter can affect negatively the blade performance even it can cause to redesign the blade. In modern blade, preventing flutter is crucial due to its effect on the long term durability of the blade structure, performance, operational safety, and energy efficiency of the system [3-7].

For many years, smart materials as piezoelectric materials have been used in blade structures. Piezoelectric materials can operate as sensors and/or actuators on a blade, respectively. They can perform as actuators and dampers to control the blade aeroelastic behaviour. In fact, implementing piezoelectric materials can avoid redesigning the blade which can significantly delay the flutter [8-9]. These materials have be implemented on active aeroelastic control of an adaptive blade [10]. They have also been used in honeycomb material [11]. Moreover, they can be implemented as vibration damping to control a plate subjected to time-dependent boundary moments and forcing function [12]. In addition, piezoelectric materials can perform as flutter controller in damaged composite laminates by employing finite element method [13]. Those materials can be used to study the aeroelastic flutter analysis on thick porous plates [14]. Moreover, piezoelectric actuators and sensors have be investigated in aeroelastic optimization [15]. The blade's aeroelastic behaviour can be effectively modified by implementing piezopatch including a shunt circuit. Previously due to the large required inductance in passive aeroelastic control, there were practical limits in the low frequency range like the one typically existing in aeroelastic phenomenon. However, nowadays having a small inductor integrated into a piezopatch can facilitate passive aeroelastic control [16]. Standard inductors are not a practical component to integrate into a piezopatch due to having too large internal resistance for resonant shunt application. It is possible to design large inductance inductors with high quality factors by using closed magnetic circuits with high permeability materials.

Damping in blade structure without causing any instability can be augmented by using shunted piezopatch. Furthermore, shunted piezopatches are simple to apply and need little to no power. Their hardware need the piezoelectrics a simple electric circuit including a capacitor, inductor, and resistor. The shunted piezopatch consumes the energy created from blade vibrations to control blade aeroelastic vibration which can reduce the vibrations of specific modes and frequencies.

In this paper, the flutter of a simple aeroelastic system speed can be increased by using piezoelectric material. The system is a 2D blade with two piezoelectric patches which has plunge DOF in the flapwise and edgewise. Later, the system is a 2D blade with piezoelectric patch which has plunge, pitch, and control rotation degrees of freedom (DOF) as well as unsteady aerodynamic forces. The objective of this work is to represent the role of piezoelectric patches that can influence substantially a simple smart blade system.

In section 2, the equations of motion of a smart blade with flapwise and edgewise plunge DOF are described how to solve those equations to obtain the flapwise and edgewise plunge velocities, displacements, electrical currents, and electric charges. Then the fixed points of the system and their stability around those points are investigated to present the system response. Example 1 shows the effective decay in the oscillation of a smart blade in comparison to a regular blade.

Section 3 shows a smart blade with the plunge, pitch, and control DOF and two piezopatches in the flapwise and edgewise plunge DOF to obtain the equations of motion under unsteady aerodynamic loads. Solving the system of equations produces the flapwise and edgewise plunge velocities, displacements, electrical currents, and electric charges as well as the pitching velocity, rotation, electrical current, and electric charge. Afterwards by obtaining the flutter speed, we indicate how adding two piezopatches can effectively defer the flutter.

In section 4, a smart blade with the plunge, pitch, and control DOF and piezopatches in the plunge and pitch DOF are presented. It shows that the flutter speed can even be further rised by having three piezopatches.

2. Aeroelastic Analysis of Smart Blade

Before investigating an aeroelastic smart blade, it requires to investigate the stability of aeroelastic smart blade. The time response of aeroelastic system can be written as [17]

$$\mathbf{x}(t) = \sum_{i=1}^{n} \mathbf{v}_i e^{\lambda_i t} b_i \tag{1}$$

where $\mathbf{v}_i$ is the smart blade spatial deformation, $e^{\lambda_i t}$ is the smart blade temporal deformation, and b_i is the eigenvector. It is a good idea to study the character of the fixed point of two DOF smart blade in the flapwise and edgewise plunge motions separately. Flapwise direction is perpendicular to the blade chord line in h_1 direction, as shown in Figure 1. In other words, flapwise direction shows the direction of the blade's instantaneous up and down displacements. However, edgewise direction shows the direction of the blade's instantaneous forward and backward displacements in h_2 direction, as shown in Figure 1.

A smart blade with only plunge DOF

Consider a smart blade which has just flapwise and edgewise plunge DOF as shown in Figure 1.

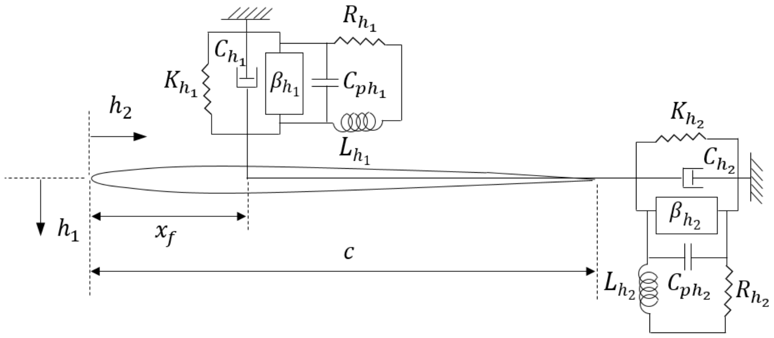

Figure 1 A smart blade with flapwise and edgewise plunge DOF

By assuming constant rotational velocity, the equations of motion for a smart blade with two plunge DOF in free vibrations can be written as below

$$\begin{cases} m\ddot{h}_1 + C_{h_1}\dot{h}_1 + K_{h_1}h_1 - \beta_{h_1}q_{h_1} = 0 \\ L_{h_1}\ddot{q}_{h_1} + R_{h_1}\dot{q}_{h_1} + \dfrac{1}{C_{ph_1}}q_{h_1} - \beta_{h_1}h_1 = 0 \\ m\ddot{h}_2 + C_{h_2}\dot{h}_2 + K_{h_2}h_2 - \beta_{h_2}q_{h_2} = 0 \\ L_{h_2}\ddot{q}_{h_2} + R_{h_2}\dot{q}_{h_2} + \dfrac{1}{C_{ph_2}}q_{h_2} - \beta_{h_2}h_2 = 0 \end{cases} \tag{2}$$

where m is the mass of smart blade, C_{h_1} is the flapwise structural damping of smart blade, K_{h_1} is the flapwise structural stiffness, h_1 is the smart blade's instantaneous flapwise displacement, β_{h_1} is the flapwise plunge electromechanical coupling, q_{h_1} is the flapwise plunge electric charge, L_{h_1} is the flapwise plunge inductance of piezoelectric material, R_{h_1} is the flapwise plunge resistance of piezoelectric material, C_{ph_1} is the flapwise plunge capacitance of piezoelectric material, C_{h_2} is the edgewise structural damping of smart blade, K_{h_2} is the edgewise structural stiffness, h_2 is the smart blade's instantaneous edgewise displacement, β_{h_2} is the edgewise plunge electromechanical coupling, q_{h_2} is the edgewise plunge electric charge, L_{h_2} is the edgewise plunge inductance of piezoelectric material, R_{h_2} is the edgewise plunge resistance of piezoelectric material, and C_{ph_2} is the edgewise plunge capacitance of piezoelectric material. As mentioned before, the flapwise plunge electromechanical coupling can be obtained as $\beta_{h_1} = e_{h_1}/C_{ph_1}$ where

e_{h_1} is the flapwise plunge coupling coefficient and the edgewise plunge electromechanical coupling can be obtained as $\beta_{h_2} = e_{h_2}/C_{ph_2}$ where e_{h_2} is the edgewise plunge coupling coefficient. Considering $x_1 = \dot{h}_1,\ x_2 = h_1,\ x_3 = \dot{q}_{h_1},\ x_4 = q_{h_1},\ x_5 = \dot{h}_2,\ x_6 = h_2,\ x_7 = \dot{q}_{h_2}$, and $x_8 = q_{h_2}$, Eq. (2) can be written as first-order differential equations

$$\begin{cases} \dot{x}_1 = -\dfrac{C_{h_1}}{m}x_1 - \dfrac{K_{h_1}}{m}x_2 + \dfrac{\beta_{h_1}}{m}x_4 \\ \dot{x}_2 = x_1 \\ \dot{x}_3 = -\dfrac{R_{h_1}}{L_{h_1}}x_3 - \dfrac{1}{C_{ph_1}L_{h_1}}x_4 + \dfrac{\beta_{h_1}}{L_{h_1}}x_1 \\ \dot{x}_4 = x_3 \\ \dot{x}_5 = -\dfrac{C_{h_2}}{m}x_5 - \dfrac{K_{h_2}}{m}x_6 + \dfrac{\beta_{h_2}}{m}x_8 \\ \dot{x}_6 = x_5 \\ \dot{x}_7 = -\dfrac{R_{h_2}}{L_{h_2}}x_7 - \dfrac{1}{C_{ph_2}L_{h_2}}x_8 + \dfrac{\beta_{h_2}}{L_{h_2}}x_6 \\ \dot{x}_8 = x_7 \end{cases} \tag{3}$$

Defining $\boldsymbol{q} = [m \quad C_{h_1} \quad K_{h_1} \quad \beta_{h_1} \quad L_{h_1} \quad R_{h_1} \quad C_{ph_1} \quad C_{h_2} \quad K_{h_2} \quad \beta_{h_2} \quad L_{h_2} \quad R_{h_2} \quad C_{ph_2}]^T$ and $\mathbf{x} = [x_1 \quad x_2 \quad x_3 \quad x_4 \quad x_5 \quad x_6 \quad x_7 \quad x_8]^T$, Eq. (3) can be written as

$$\dot{\mathbf{x}} = \mathbf{f}(\mathbf{x}, \boldsymbol{q}) = \begin{bmatrix} -\dfrac{C_{h_1}}{m}x_1 - \dfrac{K_{h_1}}{m}x_2 + \dfrac{\beta_{h_1}}{m}x_4 \\ x_1 \\ -\dfrac{R_{h_1}}{L_{h_1}}x_3 - \dfrac{1}{C_{ph_1}L_{h_1}}x_4 + \dfrac{\beta_{h_1}}{L_{h_1}}x_2 \\ x_3 \\ -\dfrac{C_{h_2}}{m}x_5 - \dfrac{K_{h_2}}{m}x_6 + \dfrac{\beta_{h_2}}{m}x_8 \\ x_5 \\ -\dfrac{R_{h_2}}{L_{h_2}}x_7 - \dfrac{1}{C_{ph_2}L_{h_2}}x_8 + \dfrac{\beta_{h_2}}{L_{h_2}}x_6 \\ x_7 \end{bmatrix} \tag{4}$$

where $\mathbf{f}$ represents linear functions, and $x_1,\ x_2,\ x_3,\ x_4,\ x_5,\ x_6,\ x_7$, and x_8 are the smart blade states and represent the system's flapwise velocity, flapwise displacement, flapwise electrical current, flapwise electric charge responses, edgewise velocity, edgewise displacement, edgewise electrical current, and edgewise electric charge responses, respectively. The two DOF aeroelastic smart blade system has eight eigenvalues that explain the stability of the fixed point. The fixed points, or static solutions, of the system are calculated from the solutions of

$$\mathbf{f}(\mathbf{x}, \boldsymbol{q}) = \mathbf{0} \tag{5}$$

or, equivalently,

$$\dot{\mathbf{x}} = \mathbf{0} \tag{6}$$

By considering Eq. (4), Eq. (6) can be presented as

$$\dot{\mathbf{x}} = \boldsymbol{A}(\boldsymbol{q})\mathbf{x} \tag{7}$$

where

$$\boldsymbol{A}=\begin{bmatrix} -\frac{C_{h_1}}{m} & -\frac{K_{h_1}}{m} & 0 & \frac{\beta_{h_1}}{m} & 0 & 0 & 0 & 0 \\ 1 & 0 & 0 & 0 & 0 & 0 & 0 & 0 \\ 0 & \frac{\beta_{h_1}}{L_{h_1}} & -\frac{R_{h_1}}{L_{h_1}} & -\frac{1}{C_{ph_1}L_{h_1}} & 0 & 0 & 0 & 0 \\ 0 & 0 & 1 & 0 & 0 & 0 & 0 & 0 \\ 0 & 0 & 0 & 0 & -\frac{C_{h_2}}{m} & -\frac{K_{h_2}}{m} & 0 & \frac{\beta_{h_2}}{m} \\ 0 & 0 & 0 & 0 & 1 & 0 & 0 & 0 \\ 0 & 0 & 0 & 0 & 0 & \frac{\beta_{h_2}}{L_{h_2}} & -\frac{R_{h_2}}{L_{h_2}} & -\frac{1}{C_{ph_2}L_{h_2}} \\ 0 & 0 & 0 & 0 & 0 & 0 & 1 & 0 \end{bmatrix} \tag{8}$$

The solution of Eq. (7) can be written [2]

$$\mathbf{x}(t)=\sum_{i=1}^{n}\mathbf{v}_i e^{\lambda_i t} b_i \tag{9}$$

where $\mathbf{v}_i$ is the ith eigenvector of $\boldsymbol{A}$, λ_i is the ith eigenvalue of $\boldsymbol{A}$, and b_i is the ith element of $\boldsymbol{b}=\boldsymbol{V}^{-1}\mathbf{x}_0$, where $\boldsymbol{V}$ is the eigenvector of $\boldsymbol{A}$ and $\mathbf{x}_0$ is the initial condition.

Example 1 A smart blade with flapwise and edgewise plunge DOF in system response

As the first example, a smart blade with only flapwise and edgewise plunge DOF, Figure 1, has been considered which has the following characteristics as $m=0.3872$ Kg, $C_{h_1}=0.3237$ Ns/m, $K_{h_1}=13380$ N/m, $e_{h_1}=7.55\times10^{-3}$ C/m, $C_{ph_1}=268$ nF, $L_{h_1}=106$ H, $R_{h_1}=4050\ \Omega$, $C_{h_2}=0.5$ Ns/m, $K_{h_2}=32112$ N/m, $e_{h_2}=7.55\times10^{-2}$ C/m, $C_{ph_2}=268$ nF, $L_{h_2}=106$ H, $R_{h_2}=9050\ \Omega$, and the initial conditions $x_1(0)=0$ m/s, $x_2(0)=0.1$ m, $x_3(0)=0.1$ A, $x_4(0)=0$ C, $x_5(0)=0$ m/s, $x_6(0)=0.1$ m, $x_7(0)=0$ A, and $x_8(0)=0$ C. Figure 2 depicts the system response. The solid line represents the displacement of smart blade and the dashed line shows the displacement of regular blade. As indicated in Figure 2, the vibrations can be very effectively decayed by the piezoelectric patches. Both system responses oscillate with decaying their amplitudes with time towards zero, which called as damped responses. From Figure 2, it is clear that the amplitude of the smart blade responses can decay much faster than the one of the regular blade responses. The oscillation of smart blade flapwise, Figure 2 (a), decays almost 0.6 s however, the oscillation of the regular blade takes around 12 s to decay. Moreover, the oscillation of smart blade edgewise, Figure 2 (b), decays 0.5 s however, the oscillation of the regular blade takes around 10 s to decay.

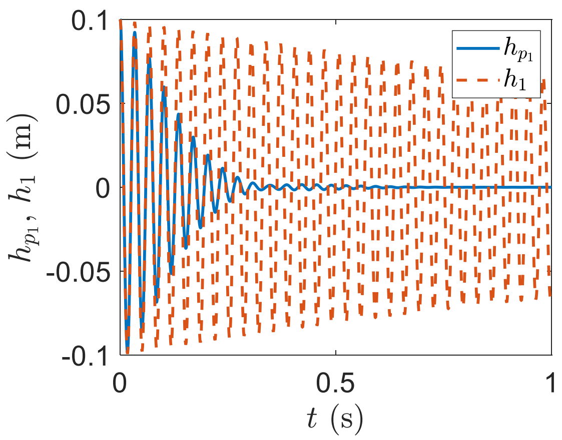

(a) Flapwise

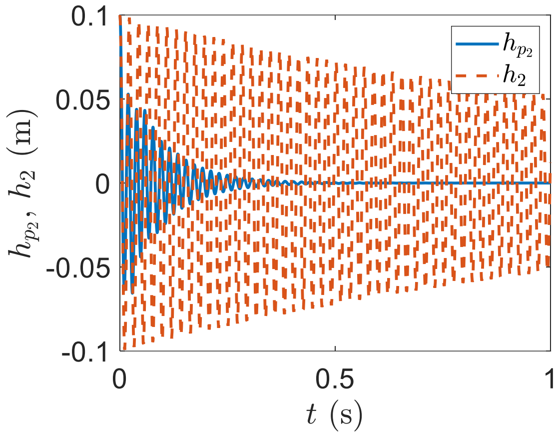

(b) Edgewise

Figure 2 Smart blade system responses

Furthermore, the phase plane plot for the velocities and displacements depict the point (0,0) recalls the system trajectory, as shown in Figure 3. The trajectories of smart blade flapwise and edgewise start from the initial displacements and velocities at the far right and it is turning to the center of the phase plane where (0,0) is the fixed point, $\boldsymbol{x}_F = \boldsymbol{0}$. In fact, the phase plane plots indicate that the fixed points draw the smart blade trajectories.

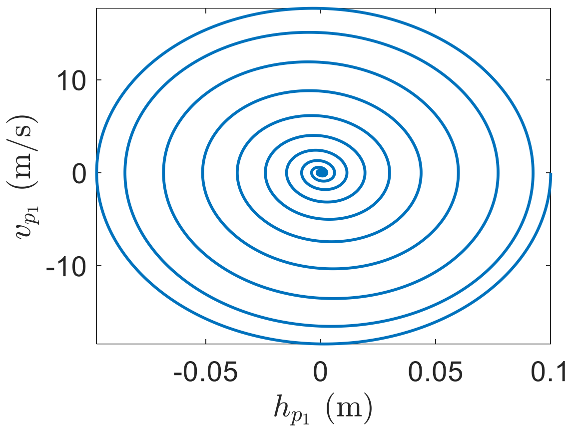

(a) Flapwise

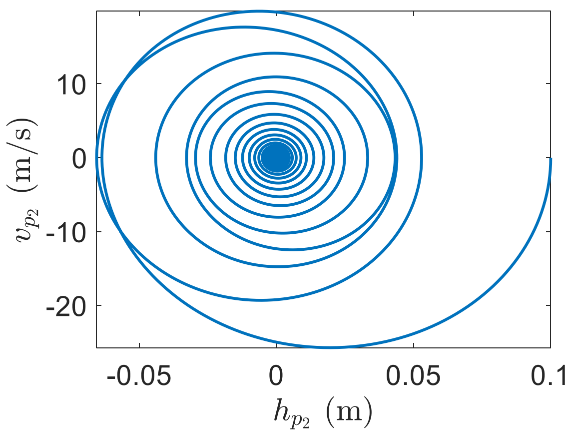

(b) Edgewise

Figure 3 Phase plane for the velocity and displacement

Likewise, the electrical current and charge phase plane start at the electrical current and charge initial conditions which are zeros and they are turning out counter-clockwise until arriving at maximum values. The trajectories then turn towards the start point (0,0), as shown in Figure 4.

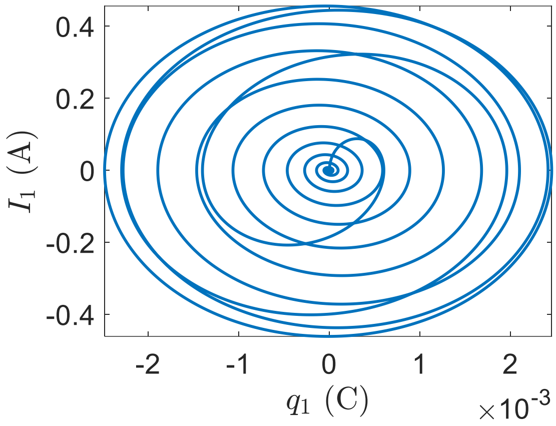

(a) Flapwise

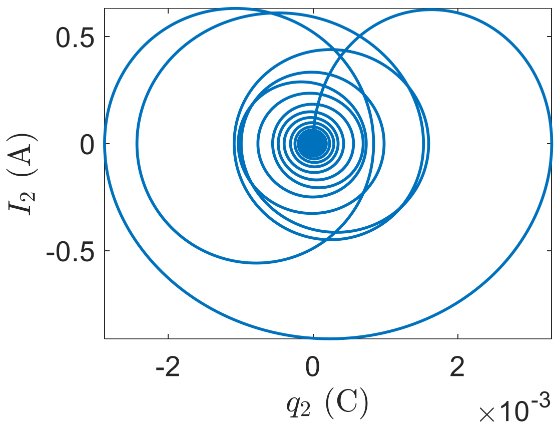

(b) Edgewise

Figure 4 Phase planes for the electrical current and charge

3. Smart Blade with Plunge, Pitch and Control DOF and piezopatches in plunge DOF

Figure 5 depicts a 2D smart blade which has plunge, pitch, and control degrees of freedom. In the model, there are an airfoil with two piezoelectric patches in the flapwise and edgewise plunge DOF. The system includes the flapwise and edgewise plunge, pitch, and control degrees of freedom (DOF) indicated by h_1, h_2, α, and β, respectively. The angle of the control surface around its hinge, located at distance x_h from the leading edge, has been represented by the DOF β and the stiffness of the control surface has been denoted by K_β.

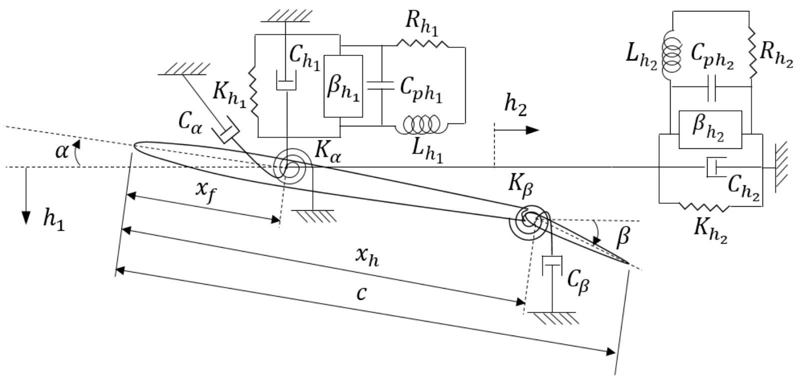

Figure 5 A smart blade with plunge, pitch, and control DOF and a piezopatch in flapwise plunge DOF

Using the Lagrange's equations and the Kirchhoff's law leads the equations of motion as

$$\begin{cases} m\ddot{h}_1 + S_{\alpha h}\ddot{\alpha} + S_\beta\ddot{\beta} + C_{h_1}\dot{h}_1 + K_{h_1}h_1 - \beta_{h_1}q_{h_1} = -L \\ S_{\alpha h}\ddot{h}_1 + I_\alpha\ddot{\alpha} + I_{\alpha\beta}\ddot{\beta} + C_\alpha\dot{\alpha} + K_\alpha\alpha = M_{xf} \\ S_\beta\ddot{h}_1 + I_{\alpha\beta}\ddot{\alpha} + I_\beta\ddot{\beta} + C_\beta\dot{\beta} + K_\beta\beta = M_{xh} \\ L_{h_1}\ddot{q}_{h_1} + R_{h_1}\dot{q}_{h_1} + \dfrac{1}{C_{ph_1}}q_{h_1} - \beta_{h_1}h_1 = 0 \\ m\ddot{h}_2 + C_{h_2}\dot{h}_2 + K_{h_2}h_2 - \beta_{h_2}q_{h_2} = 0 \\ L_{h_2}\ddot{q}_{h_2} + R_{h_2}\dot{q}_{h_2} + \dfrac{1}{C_{ph_2}}q_{h_2} - \beta_{h_2}h_2 = 0 \end{cases} \tag{10}$$

where m, C_{h_1}, K_{h_1}, h_1, β_{h_1}, q_{h_1}, L_{h_1}, R_{h_1}, C_{ph_1}, C_{h_2}, K_{h_2}, h_2, β_{h_2}, q_{h_2}, L_{h_2}, R_{h_2}, and C_{ph_2} are defined as in Eq. (2), $S_{\alpha h}$ is the static mass moment of the blade around the pitch axis x_f, I_α is the mass moment of inertia around the pitch axis x_f, S_β is the static mass moment of the control surface around the hinge axis x_h, I_β is the control surface moment of inertia around the hinge axis, $I_{\alpha\beta}$ is the product of inertia of the blade and control surface, L is the lift, M_{xf} is pitching moment of the blade around the pitch axis x_f, M_{xh} is the pitching moment of the control surface around the hinge axis x_h. Considering unsteady aerodynamics, the lift and moments can be written as follows [17-18]

$$\begin{gathered} L(t) = \rho b^2\left(U\pi\dot{\alpha} + \pi\ddot{h} - \pi ba\ddot{\alpha} - UT_4\dot{\beta} - T_1 b\ddot{\beta}\right) \\ +2\pi\rho bU\left(\Phi(0)w - \int_0^t \frac{\partial\Phi(t-t_0)}{\partial t_0}w(t_0)dt_0\right) \end{gathered} \tag{11}$$

$$\begin{gathered} M_{xf} = -\rho b^2\left(-a\pi b\ddot{h} + \pi b^2\left(\frac{1}{8} + a^2\right)\ddot{\alpha} - (T_7 + (c_h - a)T_1)b^2\ddot{\beta}\right) \\ -\rho b^2\left(\pi\left(\frac{1}{2} - a\right)Ub\dot{\alpha} + \left(T_1 - T_8 - (c_h - a)T_4 + \frac{T_{11}}{2}\right)Ub\dot{\beta}\right) - \rho b^2(T_4 + T_{10})U^2\beta \\ +2\rho Ub^2\pi\left(a + \frac{1}{2}\right)\left(\Phi(0)w - \int_0^t \frac{\partial\Phi(t-t_0)}{\partial t_0}w(t_0)dt_0\right) \end{gathered} \tag{12}$$

$$\begin{gathered} M_{xh} = -\rho b^2\left(-T_1 b\ddot{h} + 2T_{13}b^2\ddot{\alpha} - \frac{1}{\pi}T_3 b^2\ddot{\beta}\right) \\ -\rho b^2\left(\left(-2T_9 - T_1 + T_4\left(a - \frac{1}{2}\right)\right)Ub\dot{\alpha} - \frac{1}{2\pi}UbT_4T_{11}\dot{\beta}\right) \\ -\frac{\rho b^2U^2}{\pi}(T_5 - T_4T_{10})\beta - \rho b^2UT_{12}\left(\Phi(0)w - \int_0^t \frac{\partial\Phi(t-t_0)}{\partial t_0}w(t_0)dt_0\right) \end{gathered} \tag{13}$$

Substituting Eqs. (11) to (12) into Eq. (10) provides a set of equations of motion which is only time dependent and can be solved numerically like using the backward finite difference scheme for numerical integration [18]. However, the equations of motion can be given as ordinary differential equations by implementing the exponential form of Wagner function's approximation. These equations can be solved analytically rather than numerically therefore, they would be much more practical [19-20]. The Wagner function's approximation can be presented as

$$\Phi(t) = 1 - \Psi_1 e^{-\varepsilon_1 Ut/b} - \Psi_2 e^{-\varepsilon_2 Ut/b} \tag{14}$$

where $\Psi_1 = 0.165$, $\Psi_2 = 0.335$, $\varepsilon_1 = 0.0455$, and $\varepsilon_2 = 0.3$.

The full unsteady aeroelastic equations of motion can be given as follows

$$\begin{gathered} (\boldsymbol{A} + \rho\boldsymbol{B})\ddot{\boldsymbol{y}} + (\boldsymbol{C} + \rho U\boldsymbol{D})\dot{\boldsymbol{y}} + (\boldsymbol{E} + \rho U^2\boldsymbol{F})\boldsymbol{y} + \rho U^3\boldsymbol{W} = \rho U\mathbf{g}\dot{\Phi}(t) \\ \dot{\boldsymbol{w}} - \boldsymbol{W}_1\boldsymbol{y} - U\boldsymbol{W}_2\boldsymbol{w} = 0 \end{gathered} \tag{15}$$

where $\boldsymbol{y} = [h_1 \quad \alpha \quad \beta \quad q_{h_1} \quad h_2 \quad q_{h_2}]^T$ represents the displacement and charge vector, $\boldsymbol{w} = [w_1 \quad \cdots \quad w_6 \quad 0]^T$ gives the aerodynamic states vector, $\Phi(t)$ presents Wagner's function, $\boldsymbol{A}$ is the structural mass and inductance matrix, $\boldsymbol{B}$ represents the aerodynamic mass matrix, $\boldsymbol{C}$ is the structural damping matrix, $\boldsymbol{D}$ represents the aerodynamic damping matrix, $\boldsymbol{E}$ gives the structural stiffness and resistance matrix, $\boldsymbol{F}$ is the aerodynamic stiffness matrix, $\boldsymbol{W}$ represents the aerodynamic state influence matrix, $\mathbf{g}$ gives the initial condition excitation vector, and $\boldsymbol{W}_1$ and $\boldsymbol{W}_2$ present the aerodynamic state equation matrices.

Equations (15) can be formed in purely first order ordinary differential equations by

$$\dot{\mathbf{x}} = \boldsymbol{Q}\mathbf{x} + \mathbf{q}\dot{\Phi}(t) \tag{16}$$

where

$$\boldsymbol{Q} = \begin{bmatrix} -\boldsymbol{M}^{-1}(\boldsymbol{C} + \rho U\boldsymbol{D}) & -\boldsymbol{M}^{-1}(\boldsymbol{E} + \rho U^2\boldsymbol{F}) & -\rho U^3\boldsymbol{M}^{-1}\boldsymbol{W} \\ \boldsymbol{I}_{6\times 6} & \mathbf{0}_{6\times 6} & \mathbf{0}_{6\times 6} \\ \mathbf{0}_{6\times 6} & \boldsymbol{W}_1 & U\boldsymbol{W}_2 \end{bmatrix} \tag{17}$$

$$\mathbf{q} = \begin{pmatrix} \rho U\boldsymbol{M}^{-1}\mathbf{g} \\ \mathbf{0}_{12\times 1} \end{pmatrix} \tag{18}$$

Example 2 A smart blade with plunge, pitch, and control DOF and a piezopatch in flapwise and edgewise plunge DOF

As the second example, a smart blade with plunge, pitch, and control DOF, Figure 5, is considered with the following parameters [17]. It assumes $m = 13.5$ Kg, $S_{\alpha h} = 0.3375$ Kgm, $S_\beta = 0.1055$ Kgm, $C_{h_1} = 2.1318$ Ns/m, $K_{h_1} = 2131.8346$ N/m, $I_\alpha = 0.0787$ Kgm^2, $I_{\alpha\beta} = 0.0136$ Kgm^2, $C_\alpha = 0.1989$ Nms/rad, $K_\alpha = 198.9712$ Nm/rad, $I_\beta = 0.0044$ Kgm^2, $C_\beta = 0.0173$ Ns/m, $K_\beta = 17.3489$ N/m, $e_{h_1} = 0.145$ C/m, $C_{ph_1} = 268$ nF, $L_{h_1} = 103$ H, $R_{h_1} = 1274\ \Omega$, $K_{h_2} = 2131.8346$ N/m, $C_{h_2} = 2.1318$ Ns/m, $e_{h_2} = 0.145$ C/m, $C_{ph_2} = 2680$ nF, $L_{h_2} = 103$ H and $R_{h_2} = 1274\ \Omega$.

Running the simulation gives the flutter speed 74.2973 m/s which presents 81.41% increase in the flutter speed of a regular blade with the same characteristics without piezoelectric patches. Figure 6 depicts the variation of damping ratios of a regular blade and smart blade with respect to the airflow velocity or airspeed. It is clear that having piezoelectric patch on the blade can effectively increase the flutter speed.

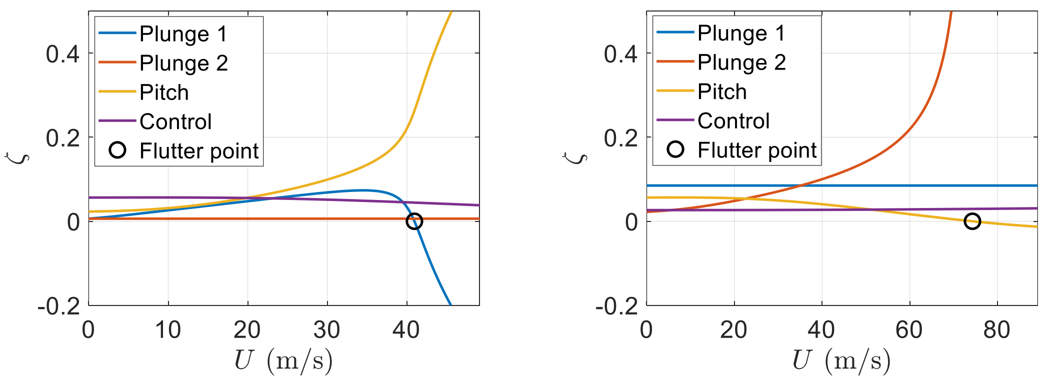

(a) (b)

Figure 6 Damping ratio versus airspeed, (a) regular blade, (b) smart blade

Furthermore, Figure 7 shows the real part of eigenvalues versus the freestream velocity. Again, Figure 7 (b) indicates the flutter speed of the smart blade can be effectively increased in comparison to the regular blade one.

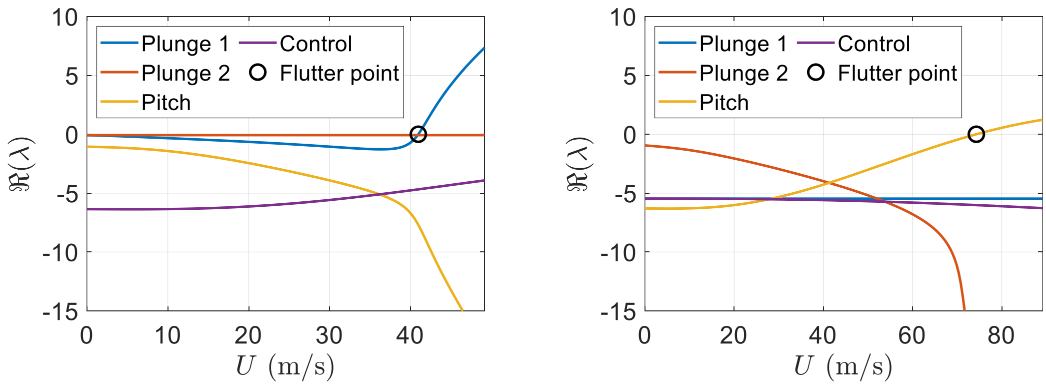

(a) (b)

Figure 7 Real part of eigenvalues versus airspeed, (a) regular blade, (b) smart blade

In addition, Figure 8 depicts the imaginary part of eigenvalues versus the freestream velocity. Figure 8 (b) indicates the flutter speed of the smart blade can be effectively increased in comparison to the regular blade one.

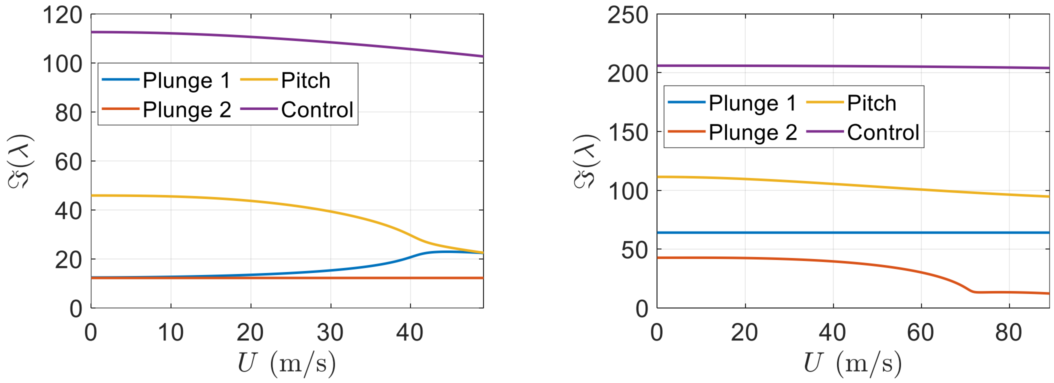

(a) (b)

Figure 8 Imaginary part of eigenvalues versus airspeed, (a) regular blade, (b) smart blade

Equation (8) can be used to form the matrix $\boldsymbol{Q}$ and its eigenvalues and eigenvectors can be obtained for two different airspeeds, $U = 10$ m/s and the flutter speed, $U = 74.2973$ m/s. The structural states dynamics of the smart blade can be represented in eight complex eigenvalues. The complex eigenvalues of the regular blade are conjugate as the complex eigenvalues of the smart blade. Six real eigenvalues belong to the aerodynamics states dynamics. Moreover, the piezoelectric states dynamics include four real eigenvalues. The first three elements of each eigenvector give the structural velocities, flapwise piezoelectric electrical current is given by the fourth element, structural displacements can be obtained from the next three elements, flapwise piezoelectric electric charge is given by the eighth element, edgewise velocity can be obtained from the ninth element, edgewise displacement can be represented by the tenth element, edgewise piezoelectric electric charge is given by the eleventh element, and finally the last next element correspond aerodynamic state displacements.

For the two structural modes, the smart blade eigenvalues at $U = 10$ m/s are as follows

$$\lambda_1 = -1.3460 \pm 42.7410i, \ \lambda_2 = -5.4698 \pm 64.0705i$$

and its corresponding eigenvectors which present the smart blade structural mode shapes are

$$\varphi_1 = \begin{Bmatrix} -0.0034 \\ 0.3795 \\ 0.9249 \\ -0.0005 \end{Bmatrix}, \varphi_2 = \begin{Bmatrix} 0.0000 \\ 0.0000 \\ 0.0000 \\ 0.0000 \end{Bmatrix}$$

where, in each mode shape, flapwise plunge displacement is presented by the first element, pitch angle can be indicated by the second element, control surface angle is presented by the third element, and edgewise plunge displacement is given by the last element. Generally, since the degrees of freedom of aeroelastic systems are coupled to each other, they cannot occur independently. Mostly, in mode one and two , there are control surface and pitch displacements. The smart blade mode one has significant pitch angle in comparison to the regular blade. Figure 9 depicts deformation of the two modes of the smart blade. In addition, the value of pitch in mode one is high however, the value of pitch in mode two is zero.

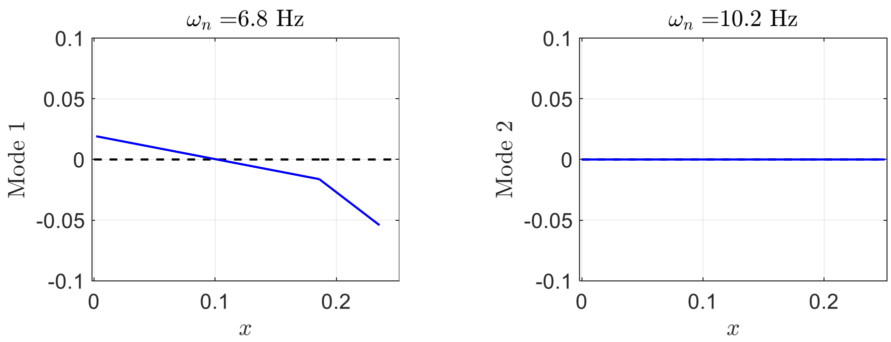

(a) (b)

Figure 9 Smart blade mode shapes of unsteady plunge-pitch-control at $U = 10$ m/s. (a) $\omega_n = 6.8$ Hz, (b) $\omega_n = 10.2$ Hz.

Furthermore, the eigenvalues of the smart blade at airspeed $U = 74.2973$ m/s can be as follows

$$\lambda_1 = -21.2035 \pm 13.2734i,\ \lambda_2 = -5.4698 \pm 64.0705i$$

and its corresponding mode shapes are

$$\varphi_1 = \begin{Bmatrix} 0.0494 \\ 0.8685 \\ -0.3664 \\ 0.0072 \end{Bmatrix}, \qquad \varphi_2 = \begin{Bmatrix} 0.0000 \\ 0.0000 \\ 0.0000 \\ 0.0000 \end{Bmatrix}$$

The real parts of λ_1 is much more negative in comparison to eigenvalues at airspeed $U = 10$ m/s. Moreover, at $U = 74.2973$ m/s, the value of mode one pitch is significant, as shown in Figure 10.

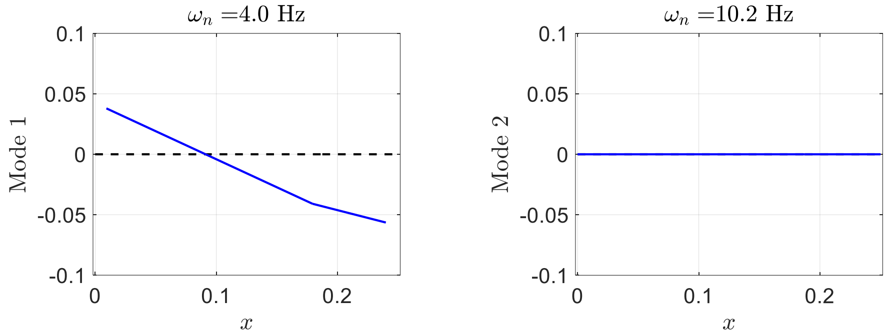

(a) (b)

Figure 10 Smart blade mode shapes of unsteady plunge-pitch-control at $U = 74.2973$ m/s. (a) $\omega_n = 4.0$ Hz, (b) $\omega_n = 10.2$ Hz.

In next section, there is a smart blade including three DOF and two piezopatches in the plunge and pitch DOF to compare its aeroelastic behaviour with a regular blade and how the flutter phenomenon can be postponed more by implementing third piezopatch on a smart blade.

4. A Smart Blade with Plunge, Pitch, and Control DOF and Piezopatches in Plunge and Pitch DOF

In this section, there is a smart blade with plunge, pitch, and control DOF in which there are three piezopatches, two in the flapwise and edgewise plunge DOF and third one in the pitch DOF, as shown in Figure 11. The same characteristics of the section three smart blade has been considered in this system.

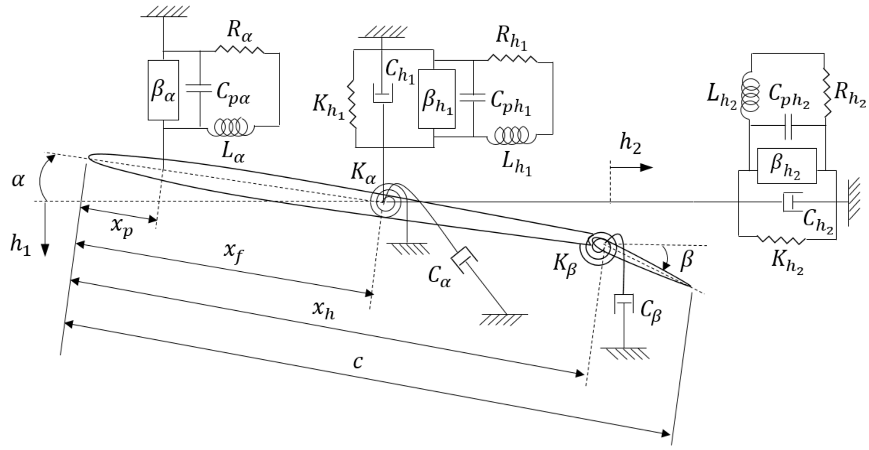

Figure 11 A smart blade with plunge, pitch, and control DOF and piezopatches in plunge and pitch DOF

The equations of motion of the smart blade can be obtained by using the Lagrange's equations and the Kirchhoff's law as

$$\begin{cases} m\ddot{h}_1 + S_{\alpha h}\ddot{\alpha} + S_\beta\ddot{\beta} + C_{h_1}\dot{h}_1 + K_{h_1}h_1 - \beta_{h_1}q_{h_1} = -L \\ S_{\alpha h}\ddot{h}_1 + I_\alpha\ddot{\alpha} + I_{\alpha\beta}\ddot{\beta} + C_\alpha\dot{\alpha} + K_\alpha\alpha - \beta_\alpha q_\alpha = M_{xf} \\ S_\beta\ddot{h}_1 + I_{\alpha\beta}\ddot{\alpha} + I_\beta\ddot{\beta} + C_\beta\dot{\beta} + K_\beta\beta = M_{xh} \\ L_{h_1}\ddot{q}_{h_1} + R_{h_1}\dot{q}_{h_1} + \dfrac{1}{C_{ph_1}}q_{h_1} - \beta_{h_1}h_1 = 0 \\ m\ddot{h}_2 + C_{h_2}\dot{h}_2 + K_{h_2}h_2 - \beta_{h_2}q_{h_2} = 0 \\ L_{h_2}\ddot{q}_{h_2} + R_{h_2}\dot{q}_{h_2} + \dfrac{1}{C_{ph_2}}q_{h_2} - \beta_{h_2}h_2 = 0 \\ L_\alpha\ddot{q}_\alpha + R_\alpha\dot{q}_\alpha + \dfrac{1}{C_{p\alpha}}q_\alpha - \beta_\alpha(x_f - x_p)\alpha = 0 \end{cases} \tag{139}$$

where m, $S_{\alpha h}$, S_β, C_{h_1}, K_{h_1}, h_1, β_{h_1}, q_{h_1}, L_{h_1}, R_{h_1}, C_{ph_1}, C_{h_2}, K_{h_2}, h_2, β_{h_2}, q_{h_2}, L_{h_2}, R_{h_2}, C_{ph_2}, L, I_α, $I_{\alpha\beta}$, C_α, K_α, M_{xf}, I_β, C_β, K_β, M_{xh}, x_f, and x_p are defined as in Eq. (10), L_α is the piezoelectric material pitch inductance, R_α is the piezoelectric material pitch resistance, $C_{p\alpha}$ is the piezoelectric material pitch capacitance, β_α is the electromechanical coupling of pitch, and q_α is the electric charge of pitch. The electromechanical coupling of pitch, β_α, depends on the coupling coefficient of pitch, e_α, and the capacitance of pitch, $C_{p\alpha}$, and it can be obtained by $\beta_\alpha = e_\alpha/C_{p\alpha}$.

The aeroelastic equations of motion in full unsteady form can be written as follows

$$\begin{gathered} (\boldsymbol{A} + \rho\boldsymbol{B})\ddot{\boldsymbol{y}} + (\boldsymbol{C} + \rho U\boldsymbol{D})\dot{\boldsymbol{y}} + (\boldsymbol{E} + \rho U^2\boldsymbol{F})\boldsymbol{y} + \rho U^3\boldsymbol{W}\boldsymbol{w} = \rho U\mathbf{g}\dot{\Phi}(t) \\ \dot{\boldsymbol{w}} - \boldsymbol{W}_1\boldsymbol{y} - U\boldsymbol{W}_2\boldsymbol{w} = 0 \end{gathered} \tag{20}$$

where $\boldsymbol{y} = [h_1 \quad \alpha \quad \beta \quad q_{h_1} \quad h_2 \quad q_{h_2} \quad q_\alpha]^T$ is the displacement and charge vector.

In order to represent Equations (20) in purely first order ordinary differential equations form, one can use the following equation

$$\dot{\mathbf{x}} = \boldsymbol{Q}\mathbf{x} + \mathbf{q}\dot{\Phi}(t) \tag{21}$$

where

$$\boldsymbol{Q} = \begin{bmatrix} -\boldsymbol{M}^{-1}(\boldsymbol{C} + \rho U\boldsymbol{D}) & -\boldsymbol{M}^{-1}(\boldsymbol{E} + \rho U^2\boldsymbol{F}) & -\rho U^3\boldsymbol{M}^{-1}\boldsymbol{W} \\ \boldsymbol{I}_{7\times7} & \mathbf{0}_{7\times7} & \mathbf{0}_{7\times6} \\ \mathbf{0}_{6\times7} & \boldsymbol{W}_1 & U\boldsymbol{W}_2 \end{bmatrix} \tag{22}$$

$$\mathbf{q} = \begin{pmatrix} \rho U\boldsymbol{M}^{-1}\mathbf{g} \\ \mathbf{0}_{13\times1} \end{pmatrix} \tag{23}$$

where $\mathbf{x} = [\dot{h}_1 \quad \dot{\alpha} \quad \dot{\beta} \quad \dot{q}_{h_1} \quad \dot{q}_\alpha \quad h_1 \quad \alpha \quad \beta \quad q_{h_1} \quad \dot{h}_2 \quad \dot{q}_{h_2} \quad h_2 \quad q_{h_2} \quad q_\alpha \quad w_1 \quad \cdots \quad w_6]^T$ is the 20×1 state vector, $\boldsymbol{M} = \boldsymbol{A} + \rho\boldsymbol{B}$, $\boldsymbol{I}_{7\times7}$ is a 7×7 unit matrix, $\mathbf{0}_{7\times7}$ is a 7×7 zero matrix, $\mathbf{0}_{7\times6}$ is a 7×6 zero matrix, $\mathbf{0}_{6\times7}$ is a 6×7 zero matrix, and $\mathbf{0}_{11\times1}$ is a 11×1 zero vector. The initial conditions are $\mathbf{x}(0) = \mathbf{x}_0$. The initial condition $\mathbf{g}\dot{\Phi}(t)$, which plays an excitation role, can decays exponentially. In this work, in order to reach steady-state solutions, the initial condition is eliminated hence Eq. (21) can be written as

$$\dot{\mathbf{x}} = \boldsymbol{Q}\mathbf{x} \tag{25}$$

Example 3 A smart blade with plunge, pitch, and control DOF and piezopatches in plunge and pitch DOF

In this example, one more piezopatch is implemented in pitch DOF of the example two smart blade to control vibrations. As shown in Figure 11, a smart blade is considered which has plunge, pitch, and control DOF. Furthermore, there are three piezopatches, two in plunge and one in pitch DOF. The smart blade has the same characteristics for the smart blade of example two. It assumes that $e_{h_1} = 0.145$ C/m, $C_{ph_1} = 2680$ nF, $L_{h_1} = 200$ H, $R_{h_1} = 2974\ \Omega$, $e_{h_2} = 0.0145$ C/m, $C_{ph_2} = 2680$ nF, $L_{h_2} = 200$ H and $R_{h_2} = 1274\ \Omega$, the parameters of pitch piezopatch as the coupling coefficient of pitch $e_\alpha = 0.00145$ C/m, the piezoelectric material pitch capacitance $C_{p\alpha} = 268$ nF, the piezoelectric material of pitch inductance $L_\alpha = 200$ H, the piezoelectric material of pitch resistance $R_\alpha = 574\ \Omega$.

Results of simulation shows that having one more piezopatch in the pitch DOF can suppress the flutter phenomenon in the pitch mode, as shown in Figure 12. Therefore, there is possibility to remove flutter in pitch DOF by possessing three piezopatches, two in the plunge DOF and one in the pitch DOF. However, the flutter phenomenon appears with higher speed in the flapwise plunge DOF.

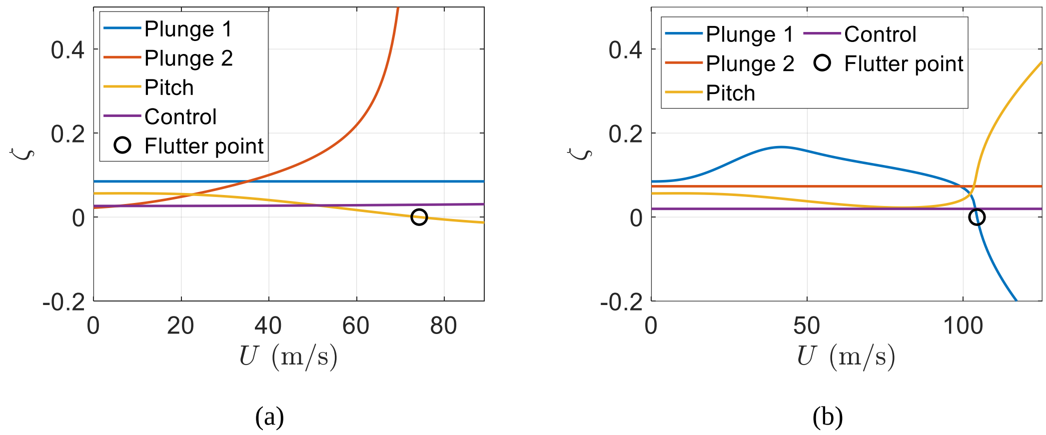

Figure 12 Smart blade damping ratio versus airspeed with, (a) plunge piezopatches, (b) plunge & pitch piezopatches

Figure 12 indicates flutter happens at 104.4198 m/s in the control DOF in the smart blade with three piezopatches. The new flutter speed value shows that it has been increased 155% in the smart blade in comparison to the one of a regular blade which has the same characteristics without piezopatch. In addition, the new flutter speed has be increased 40.54% in the smart blade in comparison to the one of a smart blade which possesses the same characteristics and only two piezopatches in the flapwise and edgewise plunge DOF. Obviously implementing three piezopatches can suppress the flutter phenomenon in the pitch mode however, it appears in the flapwise plunge mode with higher speed, as depicted in Figure 12 (b).

Moreover, Figure 13 shows the eigenvalue real parts versus the freestream velocity. Figure 13 (b) depicts clearly flutter has been removed in the pitch mode but it happens in the flapwise plunge mode with higher speed. In fact, when one piezopatch is implemented in the pitch DOF, it increases the pitching stiffness of the blade then flutter will shift from the pitch DOF to the bending DOF. It is also clear that the flutter speed of the smart blade with three piezopatches has been increased in comparison to the flutter speed of the smart blade with only two piezopatches.

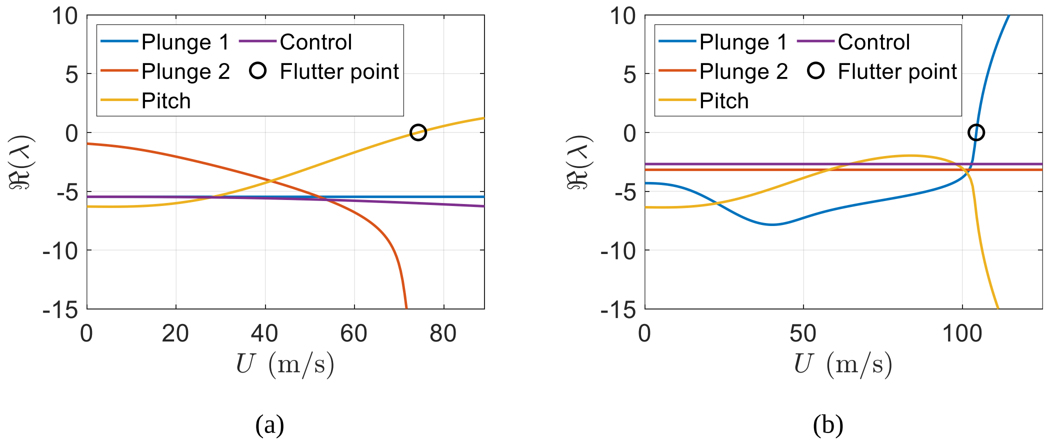

Figure 13 Real part of eigenvalues versus airspeed, (a) smart blade with plunge piezopatches, (b) smart blade with plunge & pitch piezopatches

Furthermore, Figure 14 indicates the eigenvalues imaginary parts versus the freestream velocity. According to Figure 14 (b), it is clear that flutter happens in the flapwise plunge mode and the smart blade flutter speed has been effectively increased in comparison to the regular blade one.

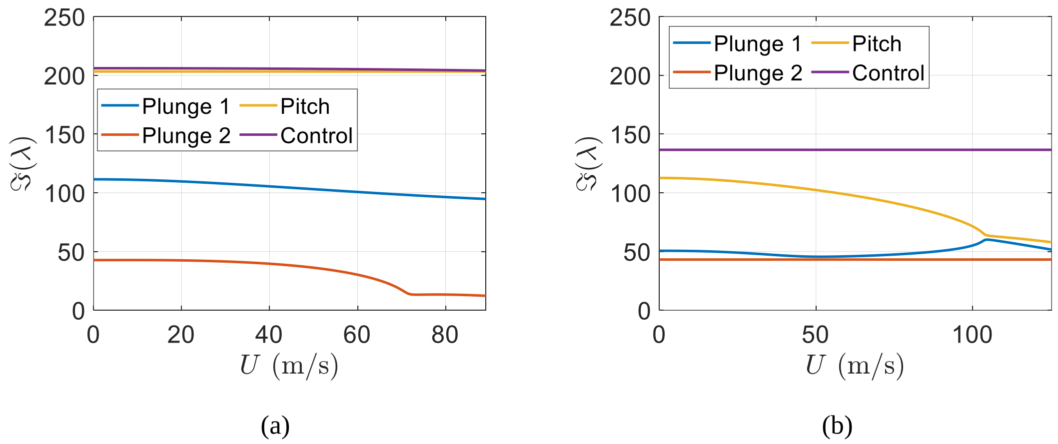

Figure 14 Imaginary part of eigenvalues versus airspeed, (a) smart blade with plunge piezopatches, (b) smart blade with plunge & pitch piezopatches

Equation (16) can be used to form the matrix $\boldsymbol{Q}$ then its eigenvalues and eigenvectors can be obtained for two different airspeeds, $U = 10$ m/s and the flutter speed, $U = 104.4198$ m/s. The smart blade structural states dynamics can be represented by eight complex eigenvalues. Similar to the regular blade eigenvalues, these complex eigenvalues are conjugate. Six real eigenvalues are for the aerodynamics states dynamics. Moreover, six real eigenvalues represent the piezoelectric states dynamics. The first four eigenvector elements provide structural velocities, the next four elements give structural displacements, the next six elements provide aerodynamic state displacements, and finally the last six elements correspond to piezoelectric electric charges.

At $U = 10$ m/s, the eigenvalues of smart blade for the two structural modes can be as follows

$$\lambda_1 = -22.0865 \pm 1.4051i, \ \lambda_2 = -0.0863 \pm 11.9886i$$

and their corresponding eigenvectors can represent the smart blade structural mode shapes as

$$\varphi_1 = \begin{Bmatrix} -0.3729 \\ 0.3119 \\ 0.8688 \\ -0.0498 \end{Bmatrix}, \qquad \varphi_2 = \begin{Bmatrix} 0.0000 \\ 0.0000 \\ 0.0000 \\ 0.0000 \end{Bmatrix}$$

where, in each mode shape, the first element provides plunge displacement of flapwise, the second element presents pitch angle, the third element indicates control surface angle, and the last element provides plunge displacement of edgewise. The degrees of freedom of aeroelastic systems are generally coupled to each other and cannot appear independently. Mainly, flapwise plunge displacement, pitch, and control surface angles happen in mode one. Mode one contains significant positive control surface angle. Figure 15 shows the deformation of the smart blade in the two modes. Clearly similarity almost exists in pitch and control with opposite signs in modes one.

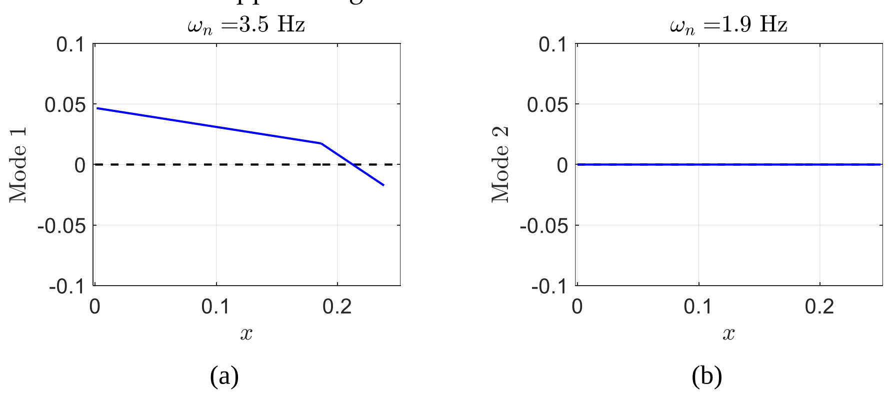

Figure 15 Smart blade mode shapes of unsteady plunge-pitch-control at $U = 10$ m/s. (a) $\omega_n = 3.5$ Hz, (b) $\omega_n = 1.9$ Hz.

Furthermore, at airspeed $U = 104.4198$ m/s, the smart blade eigenvalues can be

$$\lambda_1 = -0.0863 \pm 11.9886i, \ \lambda_2 = -3.1737 \pm 43.1479i$$

and their corresponding mode shapes are as

$$\varphi_1 = \begin{Bmatrix} 0.0000 \\ 0.0000 \\ 0.0000 \\ 0.0000 \end{Bmatrix}, \qquad \varphi_2 = \begin{Bmatrix} 0.0000 \\ 0.0000 \\ 0.0000 \\ 0.0000 \end{Bmatrix}$$

The real part of λ_2 is much closer in comparison to eigenvalues at airspeed $U = 10\ \mathrm{m/s}$ and the real part of λ_1 is almost zero. In addition, at $U = 104.4198\ \mathrm{m/s}$, all mode shape components of φ_1 and φ_2 become almost zero, as depicted in Figure 16.

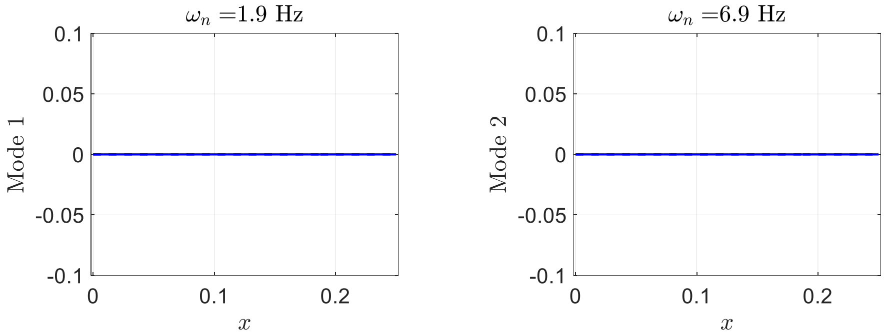

(a) (b)

Figure 16 Smart blade mode shapes of unsteady plunge-pitch-control at $U = 104.4198\ \mathrm{m/s}$. (a) $\omega_n = 1.9$ Hz, (b) $\omega_n = 6.9$ Hz.

5. Conclusion

In this paper, it has been shown how by using piezoelectric patches, the flutter phenomenon can be postponed on a smart blade. Section 2 represents system response of a smart blade with only plunge DOF. Clearly, the oscillations of the smart blade can be effectively decayed in a very short time by implementing efficient flapwise and edgewise piezopatches. Almost in 0.6 s, the vibration of the smart blade with only plunge DOF can be decayed however, the vibration of the regular blade without piezoelectric patch needs around 12 s to decay. As illustrated in section 3, by using two piezopatches in the flapwise and edgewise plunge DOF of a regular blade with three DOF, the flutter speed can be postponed 81.41% which shows that the flutter speed has been increased in a considerable value. Moreover, it shows that how the flutter phenomenon can shift from the flapwise plunge mode in a regular blade to the pitch mode in a smart blade. Later, it presents the effect of adding one more piezopatch to a smart blade in the pitch DOF to postpone more the flutter phenomenon. The flutter speed in a smart blade can be postponed 155% which is a very considerable value.

Funding Acknowledgement
This research received no specific grant from any funding agency in the public, commercial, or not-for-profit sectors.

Conflict of Interest Statement
The authors declare no conflict of interest in preparing this article.

References

1. Nguyen, N.T.; Ting, E.; Lebofsky, S. *Aeroelastic Analysis of a Flexible Wing Wind Tunnel Model with Variable Camber Continuous Trailing Edge Flap Design*; AIAA 2015-1405; American Institute of Aeronautics and Astronautics; 2015.
2. Hallissy, B.P.; Cesnik, C.E.S. *High-Fidelity Aeroelastic Analysis of Very Flexible Aircraft*; AIAA 2011-1914; American Institute of Aeronautics and Astronautics; 2011.
3. Bisplinghoff, R.L.; Ashley H.; Halfman R.L. et al. *Aeroelasticity*; Republication; Dover Publications; New York; USA; 1996.
4. Fung, Y.C. *An Introduction to the Theory of Aeroelasticity*; Republication; Dover Publications; New York; USA; 2008.
5. Dowell, E.H. *A Modern Course in Aeroelasticity*, 5th ed.; Springer International Publishing: Switzerland, 2015.
6. Hodges, D.H.; Pierce, G.A. *Introduction to Structural Dynamics and Aeroelasticity*, 2nd ed.; Cambridge University Press: 2011.
7. Wright, J.R.; Cooper, J.E. *Introduction to Aircraft Aeroelasticity and Loads*, 2nd ed.; John Wiley & Sons, Ltd.; USA; 2015.
8. Moosavi, R.; Elasha, F. *Smart Wing Flutter Suppression*, Designs, 2022, 6(2), 29.
9. Verstraelen, E.; Gaëtan, K.; Grigorios, D. Flutter and Limit Cycle Oscillation Suppression Using Linear and Nonlinear Tuned Vibration Absorbers. In *Proceedings of the SEM IMAC XXXV*; 2017.

10. Rocha, J.; Moniz, P.A.; Costa, A.P.; Suleman, A. On Active Aeroelastic Control of an Adaptive Wing Using Piezoelectric Actuators. *J. Aircr.* **2005**, *42*, 278–282.
11. Olympio, K.R.; Poulin-Vittrant, G. *A Honeycomb-Based Piezoelectric Actuator for a Flapping Wing MAV*; SPIE Smart Structures and Materials, Nondestructive Evaluation and Health Monitoring: San Diego, CA, USA, 2011.
12. Kucuk, I.; Yıldırım, K.; Adali, S. Optimal piezoelectric control of a plate subject to time-dependent boundary moments and forcing function for vibration damping. *Comput. Math. Appl.* **2015**, *69*, 291–303.
13. Kuriakose, V.M.; Sreehari, V. Study on passive flutter control of damaged composite laminates with piezoelectric patches employing finite element method. *Compos. Struct.* **2021**, *269*, 114021.
14. Bahaadini, R.; Saidi, A.R.; Majidi-Mozafari, K. Aeroelastic Flutter Analysis of Thick Porous Plates in Supersonic Flow. *Int. J. Appl. Mech.* **2019**, *11*.
15. Muc, A.; Flis, J.; Augustyn, M. Optimal Design of Plated/Shell Structures under Flutter Constraints—A Literature Review. *Materials* **2019**, *12*, 4215.
16. Lossouarn, B.; Aucejo, M.; Deü, J.-F.; Multon, B. Design of inductors with high inductance values for resonant piezoelectric damping. *Sensors Actuators A Phys.* **2017**, *259*, 68–76.
17. Dimitriadis, G. *Introduction to Nonlinear Aeroelasticity*; Wiely; USA; 2017.
18. Theodorsen, T. General Theory of Aerodynamic Instability and the Mechanism of Flutter. *NASA. Ames Res. Cent. Class. Aerodyn. Theory* **1934**, 291–311.
19. Lee, B.; Price, S.; Wong, Y. Nonlinear aeroelastic analysis of airfoils: bifurcation and chaos. *Prog. Aerosp. Sci.* **1999**, *35*, 205–334.
20. Lee, B.; Gong, L.; Wong, Y. Analysis and computation of nonlinear dynamic response of a two-degree of freedom system and its application in aeroelasticity. *J. Fluids Struct.* **1997**, *11*, 225–246.